Metallic Bi and oxygen vacancy dual active sites enable efficient oxygen activation: Facet-dependent effect and interfacial synergy

Guanglan Di [a,1], Langlang Wang [a,1], Xuede Li [a,*], Xiaoli Zhao [b], Guangpeng Yang [c], Lei Huang [d], Zefang Chen [e], John Crittenden [e]

[a] *School of Resource and Environment, Anhui Agricultural University, Hefei 230036, China*
[b] *University of Chinese Academy of Sciences, Beijing 100049, China*
[c] *Rezel Catalysts Corporation, Shanghai 201313, China*
[d] *School of Environmental Science and Engineering, Guangzhou University, Guangzhou 510006, China*
[e] *Brook Byers Institute of Sustainable Systems and School of Civil and Environmental Engineering, Georgia Institute of Technology, Atlanta, GA 30332, United States*

ARTICLE INFO

ABSTRACT

Surface atomic arrangement and coordination of different crystal facets significantly affect the catalytic reactivity of photocatalysts. By modulating the solvent environment, we developed a one-step solvothermal route to synthesize a series of BiOBr nanosheets with different dominating facets ((001) and (010)) and simultaneously decorated metallic Bi and oxygen vacancies (OVs) on the identified preferred facets ((010)). The resulting Bi/OV-BiOBr-(010) outperform BiOBr-(010) with mono OVs, bare BiOBr-(010), and other well-known photocatalysts in both O_2 activation and pollutant degradation under both same catalyst loading and optical thickness conditions. The synergistic effects of the Bi-OV dual active sites in O_2 adsorption-activation and charge separation-transfer were confirmed by experimental characterization and DFT calculation. This study highlights the facet-dependent synergy of plasmonic metal-defect dual active sites and shed light on the rational design of photocatalysts for more efficient O_2 activation and refractory pollutant degradation.

1. Introduction

Advanced oxidation processes (AOPs) can efficiently remove organic pollutants by in-situ generation of reactive oxygen species (ROS), typically including both radicals (e.g., hydroxyl radical (·OH) and superoxide anion radical (·O_2^-)) and non-radicals (e.g., hydrogen peroxide (H_2O_2) and singlet oxygen ($^1O_2$)) [1–3]. However, ROS generation for most AOPs requires the addition of extra oxidants, which may result in secondary pollution [4,5]. Molecular oxygen (O_2) is one of the most economical and benign oxidants for pollutant abatement on the Earth [6]. Unfortunately, O_2 barely oxidizes pollutants under ambient conditions owing to the spin-forbidden reaction [7]. O_2 is normally in spin triplet state with two spin-unpaired outermost electrons occupied on its highest occupied molecular orbital (HOMO) orbital [8]. Differently, the HOMO orbitals of organic pollutants generally contain spin-paired electrons only, exhibiting the spin singlet characteristic [8]. According to the electronic transition selection rule, O_2 is not effective for organic pollutant degradation because of the spin-forbidden transitions of

singlet-to-triplet. Activating O_2 into ROSs is an effective strategy to utilize O_2 for recalcitrant pollutant degradation and thus attracts an increasing research interest. Noble metals [9], enzymes [10] and metalloporphyrin [11] can activate O_2 under room temperature and atmospheric pressure. Nevertheless, these materials are typically expensive or get rapidly deactivated, which would reduce the strength of O_2 as a cheap oxidant.

Photocatalysis, featured with cheap semiconductors as catalysts and solar light as the energy source, is a green and cost-effective way for O_2 activation, but it still suffers from limited efficiency because of a high electron-hole recombination rate [12,13]. Plasmonic photocatalysts, which consist of plasmonic metal and semiconductor, can efficiently improve charge separation efficiency through the surface plasmonic resonance (SPR) and Schottky effects [14]. Under light irradiation, the SPR-induced hot carriers can be injected into the adjacent semiconductor for various reactions, such as water spitting [15], CO_2 conversion [16], and environmental remediation [17], etc. Currently, most plasmonic metals adopted in plasmonic photocatalysts are noble metals,

---

such as Au [18], Ag [19], and Pd [20], etc. Considering the over expenditure of noble metals, some inexpensive metals with similar properties have been employed as substitution [21]. The plasmonic semimetal bismuth (Bi) potentially emerges as an ideal substitute for noble metals because of its unique advantages of low price, easy availability, and electron transport properties [22]. Besides the efficient charge separation, promoting O_2 adsorption on the surface of catalysts is also crucial for effective O_2 activation. Accumulative data uncovers that surface oxygen vacancies (OVs) can act as O_2 adsorption sites to boost the chemisorption of O_2 [6]. Surface OVs improve the optical and photocatalytic properties mainly because of the following three advantages. First, OVs can induce abundant localized electrons, which is beneficial for efficient O_2 activation [7]. Second, the defect states that are created by surface OVs would trap electrons or holes to inhibit charge recombination [23]. Third, the transiently charged electronic states of the adsorbates on OVs can remarkably decrease the energy barrier for interfacial charge transfer [23]. If Bi metal and OVs can be combined in a single photocatalytic system, highly enhanced photocatalytic O_2 activation and pollutant degradation can be expected. Several studies fabricated photocatalysts (such as defective Bi@BiGeO [24], Bi@OV-$Bi_2O_2CO_3$ [25], and defective Bi-metal@$Bi_2O_2[BO_2(OH)]$ [26]), which included both Bi metals and OVs, and achieved higher photocatalytic efficiencies than those with single decoration. However, most studies deposited Bi metals on OV-decorated catalysts by an extra reduction process. A facial one-step method to simultaneously introduce both Bi metals and OVs on catalysts for molecular O_2 activation is currently lacking.

Among various semiconductors, bismuth oxyhalides (BiOX, X = Cl, Br, I) has ignited considerable attention in photocatalysis due to the fascinating and tunable nanostructure. Surface OVs can be easily introduced on the BiOX nanosheets through ultraviolet light irradiation [7], hydrothermal treatment [27] or inert atmosphere calcination [28]. The photocatalytic efficiencies in various applications, such as molecular O_2 activation [7], pollutant removal [29], water splitting [30], nitrogen fixation [31], CO_2 reduction [32], and exciton dissociation [33], can be significantly boosted by the introduction of OVs. In addition, the surface atom coordination can be manipulated by adjusting the interleaving [Bi_2O_2] units and double halide atom slabs, resulting in the formation of different crystal facets with different photocatalytic activities [30]. Nevertheless, the preferred BiOBr facet was still on debate. Li et al. found that BiOBr with dominant exposed (010) exhibited better photocatalytic activity as compared to that with highly exposed (001) facets [34]. However, a contradicted conclusion was drawn by Mi et al. that BiOBr with (001) facets exhibited higher photocatalytic degradation activity than that with (001) facets [35]. More importantly, the electrons mainly transfer within the (001) bulk but on the (010) surface because of the bulk charge alternation and surface charge alternation on the respective (001) and (010) facets [14]. The facet-dependent charge transfer pattern and the open channel topology of (010) facets may allow the simultaneous creation of OVs and Bi metal on BiOBr in one step by proper material design.

Taking BiOBr as a prototype, the goals of this study are to (i) determine the preferred BiOBr facet with higher photocatalytic activity, (ii) develop a facile one-step method to fabricate BiOBr nanosheets with the exposure of the preferred facet and the decoration of Bi-OV dual active sites, and (iii) provide mechanistic understanding of the synergistic effects between metallic Bi and surface OVs. Herein, a series of BiOBr nanosheets with dominantly exposed (001) and (010) facets were synthesized via a facile solvothermal method for molecule O_2 activation and photocatalytic pollutant degradation ($\lambda > 300$ nm). The preferred BiOBr facet was determined. The synergistic mechanisms of Bi-OV dual active sites for the superior O_2 activation and pollutant degradation were systematically explored by both experimental characterization and density functional theory (DFT) calculation. This study will improve the deep understandings of facet-dependent photoreactivity and synergy of metal-OV dual active sites in boosting photoreactivity, and also provide

insights into the future structural manipulation of photocatalysts.

2. Experimental section

2.1. Chemicals

All chemicals were at least analytical-grade and used without further purification. Ultrapure water (18.2 MΩ cm^{-1}) was used throughout the experiments unless otherwise stated.

2.2. Photocatalyst preparation and characterization

(001)-facet exposed BiOBr with surface OVs (denoted as OV-BiOBr-(001)), (010)-facet exposed BiOBr with surface OVs (denoted as OV-BiOBr-(010)), and (010)-facet exposed BiOBr with surface OVs and metallic Bi (denoted as Bi/OV-BiOBr-(010)) were fabricated via a one-step solvothermal method, of which the solvents were methanol/water (1:2), ethanol/water (1:2) and ethylene glycol/water (1:2), respectively. The detailed synthetic procedures are provided in Text S1 and the simplified schematic illustration of the synthetic route is presented in Fig. S1. A reference (010)-facet exposed BiOBr without surface OVs (BiOBr-(010)) was prepared by heating OV-BiOBr-(010) at 300 C° in air for 3 h to re-oxidize the surface. For comparison, two kinds of g-C_3N_4 were synthesized by direct thermal treatment of melamine or urea at 550 C° for 3 h, and denoted as g-C_3N_4-M and g-C_3N_4-U, respectively [36]. The commercial TiO_2, ZnO and CdS photocatalysts were purchased from Shanghai Aladdin Biochemical Technology Co., Ltd. The detailed characterization methods are given in Text S2.

2.3. ROS detection

The·O_2^-,·OH and $^1O_2$ generated during the catalytic process were detected by an CIQTEK EPR200-Plus ESR spectrometer. The ESR signals of ·O_2^- and $^1O_2$ spin-trapped by DMPO were collected under illumination ($\lambda > 300$ nm), with methanol dispersion for DMPO-·O_2^- signal and aqueous dispersion for DMPO-·OH signal. $^1O_2$ generation was verified by 2,2,6,6-tetramethylpiperidine (TEMP, 10 mM) as the spin-trapping agent. The generated ·O_2^- was analyzed using nitrotetrazolium blue chloride (NBT, 2.5×10^{-5} mol/L) as the molecular probe since NBT has a maximum absorption at 259 nm while the NBT-·O_2^- products does not [12]. The generated H_2O_2 was quantified by an modified iodate method [37]. The details are provided in Text S3. The concentrations of NBT and H_2O_2 were determined by a UV–visible spectrophotometer (UV-1800PC, Shanghai Aoyi limited, China), with a maximum absorption wavelength at 259, and 351 nm, respectively. The produced·OH radicals were quantified by the 2-hrdroxyterephthalic acid (TAOH) fluorescence method [36]. Terephthalic acid (TA, 0.5 mM dissolved in 2.0 mM NaOH basic solution) can readily react with ·OH radicals to generate highly fluorescent TAOH [38]. The fluorescent intensity of TAOH, which is proportional to the concentration of ·OH radicals, was collected by a fluorescence spectrometer with excitation at 318 nm (Cary Eclipse, Agilent, Japan). The roles of different reactive species during photocatalytic process were differentiated through radical quenching experiments. EDTA-2Na (1 mM), $K_2Cr_2O_7$ (50 μM), superoxide dismutase (SOD, 1 mM), TBA (10 mM), and L-histidine (10 mM) served as the scavengers for h$^+$, e$^-$, ·O_2^-, ·OH, and $^1O_2$, respectively.

2.4. Photocatalytic activity test

Sulfamethoxazole (SMX), a widely-used broad-spectrum antibiotic, was selected as the model pollutant to evaluate the photoreactivity of the as-prepared BiOBr samples [39]. The photocatalytic reactive system is equipped with a 300 W xenon lamp (XE-JY500, Beijing NBET Technology, $\lambda > 300$ nm) in the center as the light source, surrounded by twelve quartz tubes with equal distance to the light source. All the photocatalytic experiments were conducted in the 50 mL quartz tubes at

room temperature. During illumination, all the quartz tubes rotate and revolve around the lamp at the same speed. Accordingly, all quartz tubes will receive the same lightning to ensure a fair comparison. More detailed parameters are provided in Fig. S2 and Table S1. In a typical run, 15 mg photocatalysts were dispersed in 50 mL SMX solution (5.0 mg/L). Before illumination, the suspension was stirred in dark for 30 min. During illumination, 1 mL of the solution was taken out at given time intervals and then filtered through 0.22 μm PES filters. The residual SMX was quantified by a High-Performance Liquid Chromatography (HPLC) equipped with a UV–vis detector (Agilent 1200, USA, ZORBAX ODS column). The total organic carbon (TOC) was monitored to indicate the mineralization efficiency of SMX by a Multi N/C 3100 TOC Analyzer. As for the aeration experiment, the procedures are similar to those for photodegradation experiments except that O_2 or N_2 was bubbled during the photocatalytic process.

## 2.5. Theoretical calculation

All the density functional theory (DFT) calculations were conducted using the CASTEP package in Materials studio. Geometry optimization and electronic structure properties were acquired using generalized gradient approximation (GGA) and the Perdew-Burke-Ernzerhof (PBE) exchange-correlation functions. The cut-off energy was set to 500 eV, and the structures were fully relaxed when the force was less than 0.03 eV/Å. The self-consistent-field (SCF) tolerance energy was converged to 10^{-6} eV/atom. The vacuum layer thickness of BiOBr-(001) and BiOBr-(010) slab models was maintained at 15 Å, and the Brillouin zone was sampled with a $3 \times 2 \times 1$ K points.

3. Results and discussion

3.1. Composition and structure of samples

The XRD patterns and the corresponding intensity ratios of the main facets are shown in Figs. 1a and 1b, respectively. The diffraction peaks of all samples match well with the pure tetragonal phase of BiOBr (JCPDS No. 78-0348), but the relative peak intensities of OV-BiOBr-(001) are significantly different from the other three. For OV-BiOBr-(001), the peak intensity indexed to (001), (002), (003), and (004) facets are much higher than those of the (010)-based BiOBr (including OV-BiOBr-(010), Bi/OV-BiOBr-(010), and BiOBr-(010)). Accordingly, its intensity ratios of (110), (102), and (200) to (001) are lower than those for (010)-based BiOBr. However, the intensity ratio of (002) to (200) for OV-BiOBr-(001) is 45.01, much higher than those of OV-
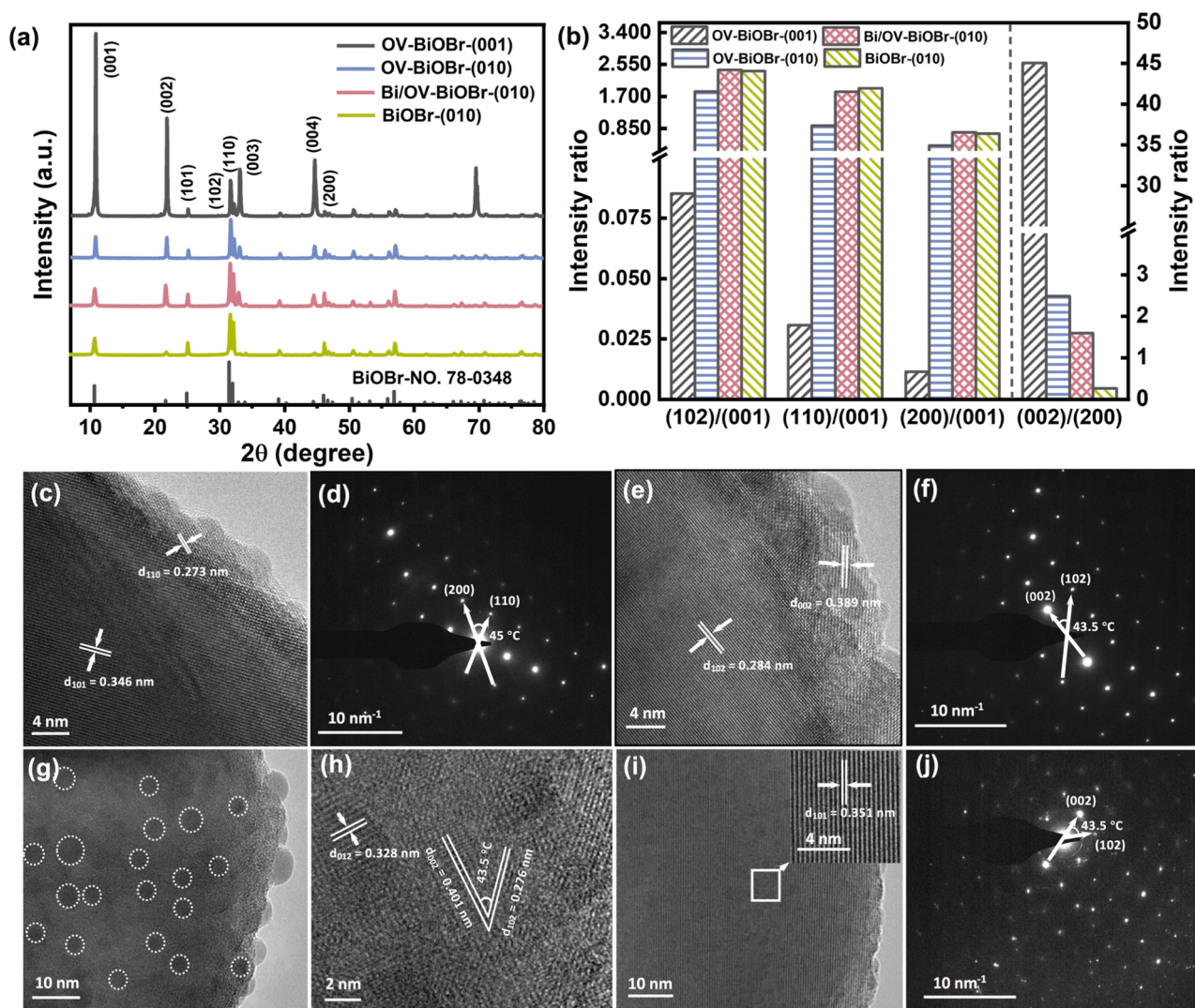
Fig. 1. (a) XRD patterns and (b) the corresponding ratios of peak intensity of BiOBr samples. (c) HR-TEM image and (d) SAED pattern of OV-BiOBr-(001). (e) HR-TEM image and (f) SAED pattern of OV-BiOBr-(010). (g) TEM image, (h) HR-TEM image on the top facet, (i) HR-TEM image on the lateral facet and (j) SAED pattern of Bi/OV-BiOBr-(010).

BiOBr-(010) (2.63), Bi/OV-BiOBr-(010) (1.79), and BiOBr-(010) (0.23). The difference in the intensity ratios reflects the difference in exposed facets. The XRD results demonstrates that OV-BiOBr-(001) dominantly exposes (001) facets, but (010)-based BiOBr samples dominantly expose (010) facets, in consistence with reported results [30,34]. The SEM images reveal that all BiOBr samples exhibit large-scale sheet-shaped structures with widths of 0.4–1.5 μm (Fig. S3). The exposed facets of the as-prepared BiOBr nanosheets were further explored by the HR-TEM. The HR-TEM image (Fig. 1c) of OV-BiOBr-(001) presents a lattice fringe of 0.273 nm, corresponding to the (110) facet, which is perpendicular to (001) facet of BiOBr. The diffraction spots in the corresponding selected area electron diffraction (SAED) demonstrates that (200) and (110) planes have inter-facet angle of ~45° (Fig. 1d) [30,40]. The value is identical to the theoretical value of angel between (200) and (110) facets. Considering the above results and the tetragonal symmetry of BiOBr, the main exposed surfaces of OV-BiOBr-(001) are identified as (001) facets. For OV-BiOBr-(010), the HRTEM image displayed two different lattice fringes with lattice spacing of 0.284 and 0.389 nm, corresponding to (102) and (002) facets, respectively (Fig. 1e). The angle between the (102) and (002) planes is ~ 43.5° (Fig. 1f). This agrees well with the theoretical value and indicates that OV-BiOBr-(010) is orientationally dominated by (010) facets. For Bi/OV-BiOBr-(010), black dots with diameters of 4–7 nm distribute uniformly in BiOBr nanosheets (Fig. 1g). The HR-TEM image on top facet demonstrate two lattice fringes with inter-lattice angle of 43.5° and lattice spacing of 0.286 and 0.401 nm, respectively (Fig. 1h). The single-crystal characteristic and the exposure of (010) facets are further supported by the SAED pattern (Fig. 1j), suggesting that Bi/OV-BiOBr-(010) is also orientationally dominated by (010) facets. Note that a new lattice fringe with lattice spacing of 0.328 nm, which corresponds to the (012) facet of Bi metals, was noticed in the black dots (Fig. 1h). Differently, no black dot was found in the HR-TEM image of the lateral facet (the lattice spacing of 0.351 nm corresponding to the BiOBr (101) facet) (Fig. 1i). These results imply that Bi metals are selectively formed on top of (010) facets of BiOBr.

3.2. Surface vacancy and band structure

XPS was conducted to investigate the surface OV of BiOBr and chemical states of Bi. As shown in Fig. 2a–d, the O 1s spectra of OV-BiOBr-(001), OV-BiOBr-(010), and Bi/OV-BiOBr-(010) demonstrate three peaks at 532.6 eV (O_a, loosely-bound O species, i.e., OH^- and H_2O), 531.4 eV (O_b, surface OVs), and 530.1 eV (O_c, Bi-O lattice oxygen), while the O 1 s spectra of BiOBr-(010) only present two peaks at

532.6 and 530.1 eV [41]. The relative intensities (%) of surface OVs for different samples are summarized in Table 1. The O_b intensity, which represents the surface OV abundance, is normally positively correlated to the O_a intensity because surface OVs will spontaneously adsorb H_2O and OH^- to lower the excess energies of surface defective sites [42]. However, Bi/OV-BiOBr-(010) had a higher O_a intensity but lower O_b intensity, compared with OV-BiOBr-(010). The abnormal phenomenon is probably resulted from the possibly generated Br vacancies (BrVs) on the surface of Bi/OV-BiOBr-(010). The BrVs may enable the spontaneous adsorption and hydroxylation as OVs do, leading to a higher O_a intensity. The nature of surface vacancies was further explored by the solid-state ESR (Fig. S4). The prominent ESR signals with g = 2.003, arose from unpaired localized electrons on surface OVs, were observed for OV-BiOBr-(001), OV-BiOBr-(010), and Bi/OV-BiOBr-(010) while the corresponding ESR signal for BiOBr-(010) is rather low, confirming the formation of surface OVs for the former three BiOBr samples. These results are consistent with the XPS results and can be again evidenced by the HR-TEM analysis (Fig. 1 and Fig. S5). Besides, Bi/OV-BiOBr-(010) exhibits a stronger ESR signal, compared with OV-BiOBr-(010), despite a lower surface OV abundance as demonstrated in the XPS results. One plausible explanation is that O and Br dual vacancies of Bi/OV-BiOBr-(010) will induce more localized electrons than the mono OVs of OV-BiOBr-(010) do. Accordingly, more unpaired localized electrons may surround the OVs of Bi/OV-BiOBr, leading to a stronger ESR signal. To validate this deduction, the intuitive evidence of BrVs is provided in SEM energy-dispersive X-ray spectroscopy (EDS) elemental mappings (Fig. S6, Table S2). According to the SEM-EDS element analysis, the atom ratios of Br/Bi and Br/(O+Bi+Br) for OV-BiOBr-(010) and Bi/OV-BiOBr-(010) are 1.392 and 0.3228, 1.319 and 0.3109, respectively. The decreased Br/Bi and Br/(O+Bi+Br) ratios are attributed to the formed BrVs of Bi/OV-BiOBr-(010). Similar results were observed for BiOCl of which the Cl/Bi ratio decreased from around 1.0–0.9 after forming Cl vacancies (ClVs) [7]. Besides, all samples show a typical spin-orbit doublet splitting located at 164.6 (Bi^{3+} $4f_{5/2}$) and 159.4 eV (Bi^{3+} $4f_{7/2}$), suggesting that the primary Bi species in BiOBr was Bi^{3+} (Fig. 2e–h) [43]. Note that an additional peak at 157. 2 eV (Bi^0 $4f_{7/2}$), the characteristic binding energy of Bi^0 in BiOBr, was noticed in Bi/OV-BiOBr-(010) [7,43]. The metallic Bi is possibly formed from the chemical reduction of Bi^{3+} by ethylene glycol solvent [41], and the partial reduction of Bi^{3+} to $Bi^{(3-x)+}$ by the localized electrons on vacancy [7]. The XPS, ESR and TEM analysis, taken together, consolidate that (i) OV-BiOBr-(001), OV-BiOBr-(010) and Bi/OV-BiOBr-(010) are all surface-defective, (ii) the OVs of Bi/OV-BiOBr-(010) with (O + Br) dual vacancies is electron-"richer" than OV-BiOBr-(010) with mono OVs, (iii)
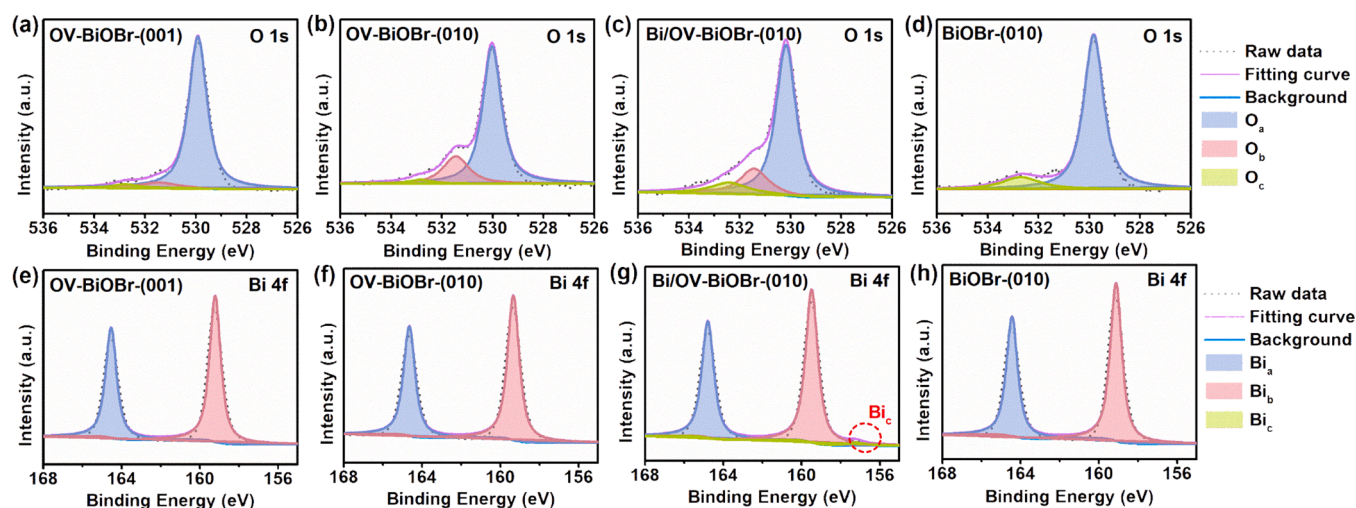

Fig. 2. High-resolution XPS spectra of O1s for (a) OV-BiOBr-(001), (b) OV-BiOBr-(010), (c) Bi/OV-BiOBr-(010), and (d) BiOBr-(010). High-resolution XPS spectra of Bi 4f for (e) OV-BiOBr-(001), (f) OV-BiOBr-(010), (g) Bi/OV-BiOBr-(010), and (h) BiOBr-(010).

Table 1
The relative intensities of surface OVs and Bi metal for different samples.

Sample	Relative intensity (%)				Relative intensity (%)		
	O_a (-OH/H_2O) (532.6 ± 0.2 eV)	O_b (O vacancy) (531.4 ± 0.1 eV)	O_c (Bi-O) (530.1 ± 0.1 eV)		Bi_a (Bi^{3+} $4f_{5/2}$) (164.6 ± 0.2 eV)	Bi_b (Bi^{3+} $4f_{7/2}$) (159.4 ± 0.2 eV)	Bi_c (Bi^0 $4f_{7/2}$) (157.2 ± 0.1 eV)
OV-BiOBr-(001)	2.6	6.1	91.3		42.8	57.2	0
OV-BiOBr-(010)	2.8	21.1	76.1		42.6	57.4	0
Bi/OV-BiOBr-(010)	9.1	16.9	74.0		42.5	55.8	1.7
BiOBr-(010)	13.4	0	86.6		42.7	57.3	0

such an electron-"richer" vacancy mode benefits the formation of metallic Bi.

A plausible mechanism for the formation of different dominant facet exposed BiOBr nanosheets was proposed (Fig. S1). First, the nucleation and growth of BiOX are sensitive to the synthetic environment [44]. The different reducing capability and viscosity of the selected solvents (ethylene > ethanol > methanol) will induce different vacancy (OV and BrV) concentrations on the layered-structured BiOBr surface [45]. When the solvent changes from methanol to ethanol and ethylene, the intensity of surface OVs increases from 6.1 % to 21.1 % and 16.9 %. When a high concentration of vacancy exists in the layered structure, the outermost surface would undergo reorganization to maintain the structural stability, allowing the appearance of different exposed facets [45]. As a result, BiOBr nanosheets are orientated along (001) direction with methanol as the solvent and along (010) direction with ethanol/-ethylene as the solvent. Besides, the migration of Bi atoms will be accompanied with the breakage of the Bi-O and Bi-Br bonds, thus the extraction of O and Br atoms can be expected on the surface of (010)

facets [45]. As for the formation of Bi-OV dual active sites, the introduction of water solvent promotes Bi^{3+} solvolysis and BiOBr nucleation, leading to an almost complete growth of the BiOBr nanosheet at the beginning of the solvothermal processes under relatively low temperatures [41]. After reaching to the high temperature, the stronger reducing capability of ethylene will induce Bi^{3+} reduction to metallic Bi [41], and thus achieves Bi deposition on the OV-decorated BiOBr surface.

Accordingly, the models of BiOBr nanosheets with dominantly exposed (001) facets and (010) facets were constructed. As can be seen, the outermost layer atoms of the (001) facest are ones of Br, O or Bi atoms (Fig. 3a, f). Differently, the (010) facets manifest an open channel characteristic, and the outermost layer is alternately arranged with Br, Bi and O atoms (Fig. 3c, h). In this way, the surface-exposed Bi atoms on the (010) facet can be easily reduced to Bi metal and deposited on the surface during the solvothermal process. The structures of BiOBr containing OVs were constructed (Fig. 3b, g for OV-BiOBr-(001), Fig. 3d, i for OV-BiOBr-(010)) by removing a O atom from the $[BiO]^+$ layer. As discussed above, metallic Bi on Bi/OV-BiOBr-(010) was partially
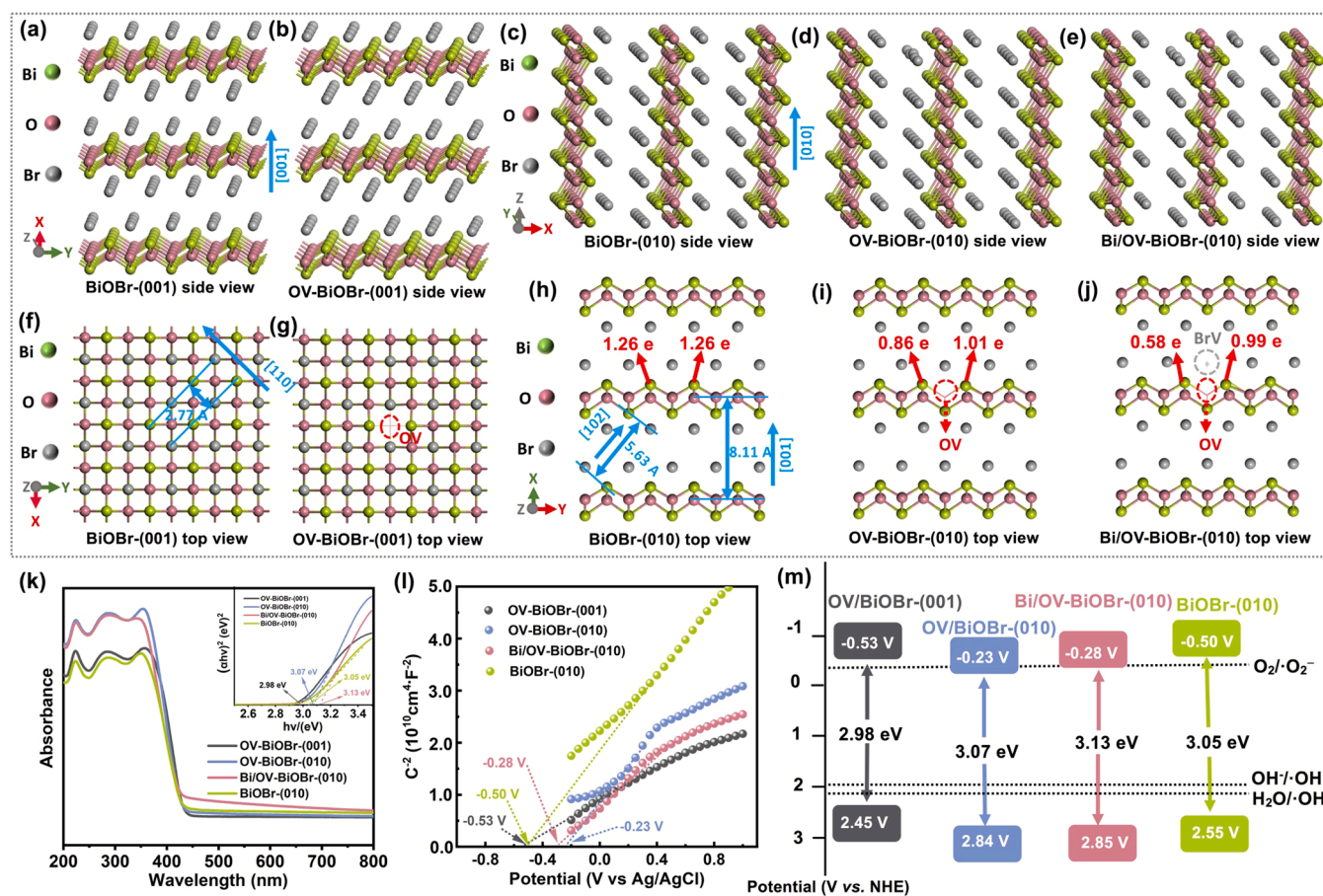
Fig. 3. (a, b) Side view and (f, g) top view of the (001) plane of the optimized local structure of BiOBr-(001) and OV-BiOBr-(001), respectively. (c, d, e) Side view and (h, i, j) top view of the (010) plane of the optimized local structure of BiOBr-(010), OV-BiOBr-(010) and Bi/OV-BiOBr-(010), respectively. (k) DRS spectra (insert is the $\alpha h\upsilon^2$ versus $h\upsilon$ curves). (l) Mott-Schottky plots. (m) Scheme of electronic band structures for all BiOBr samples.

reduced from Bi^{3+} by localized electrons on BrVs. Accordingly, the model of Bi/OV-BiOBr-(010) (Fig. 3e, j) was constructed by further removing a Br atom adjacent to OV from OV-BiOBr-(010). As illustrated in Fig. 3h–j, the Mulliken charge values of the two Bi atoms adjacent to OV in BiOBr-(010), OV-BiOBr-(010), and Bi/OV-BiOBr-(010) are in the descending order. This consists with our speculation that the co-existence of OVs and BrVs benefits the formation of Bi^0.

The effects of surface atomic arrangement and coordination on the optical absorption and the band structure of BiOBr were analyzed by UV-Vis DRS and Mott-Schottky measurements. As shown in Fig. 3k, all samples present similar absorption edges at about 450 nm. Based on the transformational Taus plots obtained from the Kubelka-Munk function (the inset of Fig. 3k), the band gap energies (E_g) of OV-BiOBr-(001), OV-BiOBr-(010) and Bi/OV-BiOBr-(010) and BiOBr-(010) were calculated to be 2.98, 3.07, 3.13, and 3.05 eV, respectively. The intercept between x-axis and the extrapolation of the straight tangent line of the Mott-Schottky plot gives the flat band potential (E_{fb}) [46]. Accordingly, E_{fb} values of OV-BiOBr-(001), OV-BiOBr-(010), Bi/OV-BiOBr-(010), and BiOBr-(010) were estimated to be − 0.53, − 0.23, − 0.28, and − 0.50 V versus Ag/AgCl (Fig. 3l, Text S5) (− 0.33, 0.23, − 0.08, and − 0.30 V versus NHE), respectively. The positive slopes of the Mott-Schottky plot suggested the n-type characteristics of BiOBr [47]. For n-type semiconductors, the E_{fb} is generally 0.1–0.3 eV higher than the conduction band potential (E_{CB}) [48]. The E_{CB} was estimated by deducting an empirical value of 0.2 V from E_{fb}. Therefore, the obtained E_{CB} for OV-BiOBr-(001), OV-BiOBr-(010), Bi/OV-BiOBr-(010), and BiOBr-(010) were − 0.53, − 0.23, − 0.28, and − 0.50 V, respectively. Accordingly, the band structures of the four BiOBr samples were determined (Fig. 3m, Table S3), revealing that molecular O_2 activation by both BiOBr-(001) and BiOBr-(010) are thermodynamically favorable.

3.3. Molecular oxygen activation

Efficient spatial separation of carries is beneficial for O_2 activation efficiency. Accordingly, the charge transfer kinetics of the as-prepared BiOBr nanosheets were investigated through transient photocurrent and electrochemical impedance spectroscopy (EIS) measurements. As shown in Fig. 4a, (010)-based BiOBr nanosheets exhibit drastically

higher photocurrent densities than that of OV-BiOBr-(001), implying the inherent higher charge separation efficiency of (010) facets. Bi/OV-BiOBr-(010) shows the highest photocurrent density, suggesting that the charge separation efficiency can be effectively boosted after metallic Bi and OVs synchronously formed on BiOBr-(010). This proposition is further supported by the remarkably reduced arc radius of Bi/OV-BiOBr-(010) in the EIS Nyquist plot (Fig. 4b). The O_2 adsorption behaviors were investigated through the temperature-programmed O_2 desorption (O_2-TPD). The desorption peak of O_2 at around 580 K is related to chemisorbed O_2 (Fig. 4c) [49]. Bi/OV-BiOBr-(010) exhibits the highest O_2 desorption peak, much higher than the second highest peak (OV-BiOBr-(010)), among all four catalysts. This indicates that metallic Bi and surface OVs synergistically enhance O_2 adsorption on the BiOBr-(010) [7].

To gain theoretical insights, density functional theory (DFT) calculations were subsequently employed to investigate the effects of metallic Bi and OVs on O_2 adsorption and activation behavior. As shown in Fig. 4d, a much more negative adsorption energy of O_2 molecule were found for OV-BiOBr-(010) (− 3.52 eV) compared to that for pure BiOBr-(010) (− 0.28 eV), revealing that OVs are the primary active sites for O_2 adsorption [49]. Bi/OV-BiOBr-(010) (− 4.34 eV) manifest a more negative O_2 adsorption energy than OV-BiOBr-(010). This implies that both Bi deposition and OV introduction favors O_2 adsorption on BiOBr-(010). Another interesting finding is that after adsorption, O_2 accepts more electrons from Bi/OV-BiOBr-(010) (− 0.57 e) and OV-BiOBr-(010) (− 0.55 e) as compared with those from pristine BMO (− 0.12 e). Consequently, the O-O bonds of O_2 after adsorption are longer for Bi/OV-BiOBr-(010) (1.55 Å) and OV-BiOBr-(010) (1.54 Å) than that for BiOBr-(010) (1.26 Å). The increased O-O bond length demonstrates that the O_2 activation for BiOBr-(010) is considerably enhanced after OV formation and Bi metal deposition. Electron density calculation was then conducted to check the relationship between the vacancy structure and electron configuration. As shown in Fig. 4e, the BrVs in Bi/OV-BiOBr-(010) would transfer part of the localized electrons to the neighboring OVs and make the OVs in Bi/OV-BiOBr-(010) electron-"richer" than the mono OVs in OV-BiOBr-(010). This result can be well supported by the Mulliken charge analysis of the Bi atoms around the OV (Table S4 and Fig. 3h–j). The Mulliken charge values of two
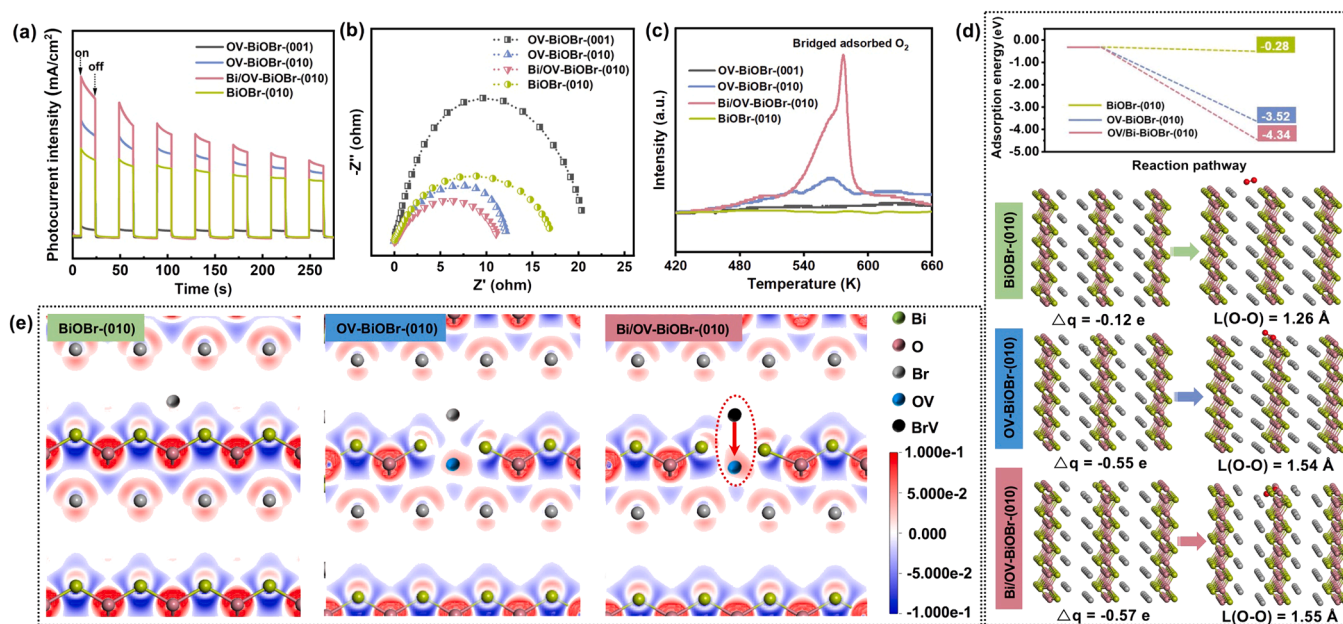
Fig. 4. Experimental characterizations and theoretical study of the O_2 activation performance: (a) Transient photocurrent responses, (b) EIS Nyquist plots and (c) O_2-TPD profiles of the as-prepared BiOBr photocatalysts. Theoretical study of the O_2 activation behavior: (d) The calculated O_2 adsorption energy, and the carried electrons (Δq) and O-O bond length ($L_{(O-O)}$) of O_2 molecules over BiOBr-(010), OV-BiOBr-(010) and Bi/OV-BiOBr-(010), respectively. (e) Charge density distribution on the surface of BiOBr-(010), OV-BiOBr-(010) and Bi/OV-BiOBr-(010).

neighing Bi atoms around the OVs in OV-BiOBr-(010) decrease from 1.26 to 1.01 and 0.86, resulting from the partial reduction of Bi^{3+} by localized electrons around OVs. When OVs coexist with BrVs in Bi/OV-BiOBr-(010), a more pronounced reduction in the Mulliken charge of Bi atoms was observed (from 1.26 to 0.99 and 0.58). These results reveal that i) the OVs in Bi/OV-BiOBr-(010) are electron-"richer" than OVs in OV-BiOBr-(010), and ii) the co-existence of OVs and BrVs are beneficial for the formation of Bi^0. Similar result was observed for BiOCl with (O + Cl) dual vacancies. The OVs in (O + Cl)Vs are electron-"richer" than the freestanding OVs, and the localized electrons on ClVs could cause the partial reduction of Bi^{3+} [7]. Such electron-"richer" OVs facilitate O_2 chemical adsorption and electron transfer for the spontaneous dissociation of O_2, consistent with the Mulliken charge results that Bi/OV-BiOBr-(010) donate more electrons to O_2 than OV-BiOBr-(010) do (Table S5).

3.4. ROS generation

The enhanced charge transfer-seperation and O_2 adsorption-activation of Bi/OV-BiOBr-(010), as discussed above, may remarkably boost the ROS generation. The generated ROS during the photocatalytic process were thus analyzed via both chemical determination and ESR detection. Generally, photocatalytic O_2 activation can generate $\cdot O_2^-$, H_2O_2, $\cdot OH$, and $^1O_2$ (Eqs. (1)–(8)). Firstly, $\cdot O_2^-$ generation was quantified by the transformation efficiency of the molecular probe NBT. As shown in Fig. 5a, (010)-facet exposed BiOBr nanosheets exhibit a higher NBT transformation efficiency over (010)-facet exposed BiOBr. Bi/OV-BiOBr-(010) shows the highest NBT transformation efficiency. This phenomenon indicates that the (010) facet favors $\cdot O_2^-$ production, and that surface OVs and Bi metal can work synergistically to further facilitate $\cdot O_2^-$ production on the (010) facet. As for H_2O_2 generation, one-step two-electron reduction of O_2 and two-step single-electron reduction of O_2 are the two possible pathways (Eqs. (1)–(4)) [12]. BiOBr-(010) surpassed Bi/OV-BiOBr-(010) and produced the highest amount of H_2O_2 (Fig. 5b). Therefore, it is speculated that H_2O_2 is mainly generated through the one-step two-electron reduction of O_2 instead of the two-step single-electron reduction [12]. Since the generated H_2O_2 can be further converted to $\cdot OH$ via Eqs. (5)–(6), the produced $\cdot OH$ was analyzed by detecting the fluorescent TAOH. The TAOH fluorescence intensity is proportional to $\cdot OH$ generation. As shown in Fig. 5c, BiOBr-(010) shows a weak fluorescence signal although it produces most H_2O_2. This implies that $\cdot OH$ may not be generated from H_2O_2 conversion. The small amount
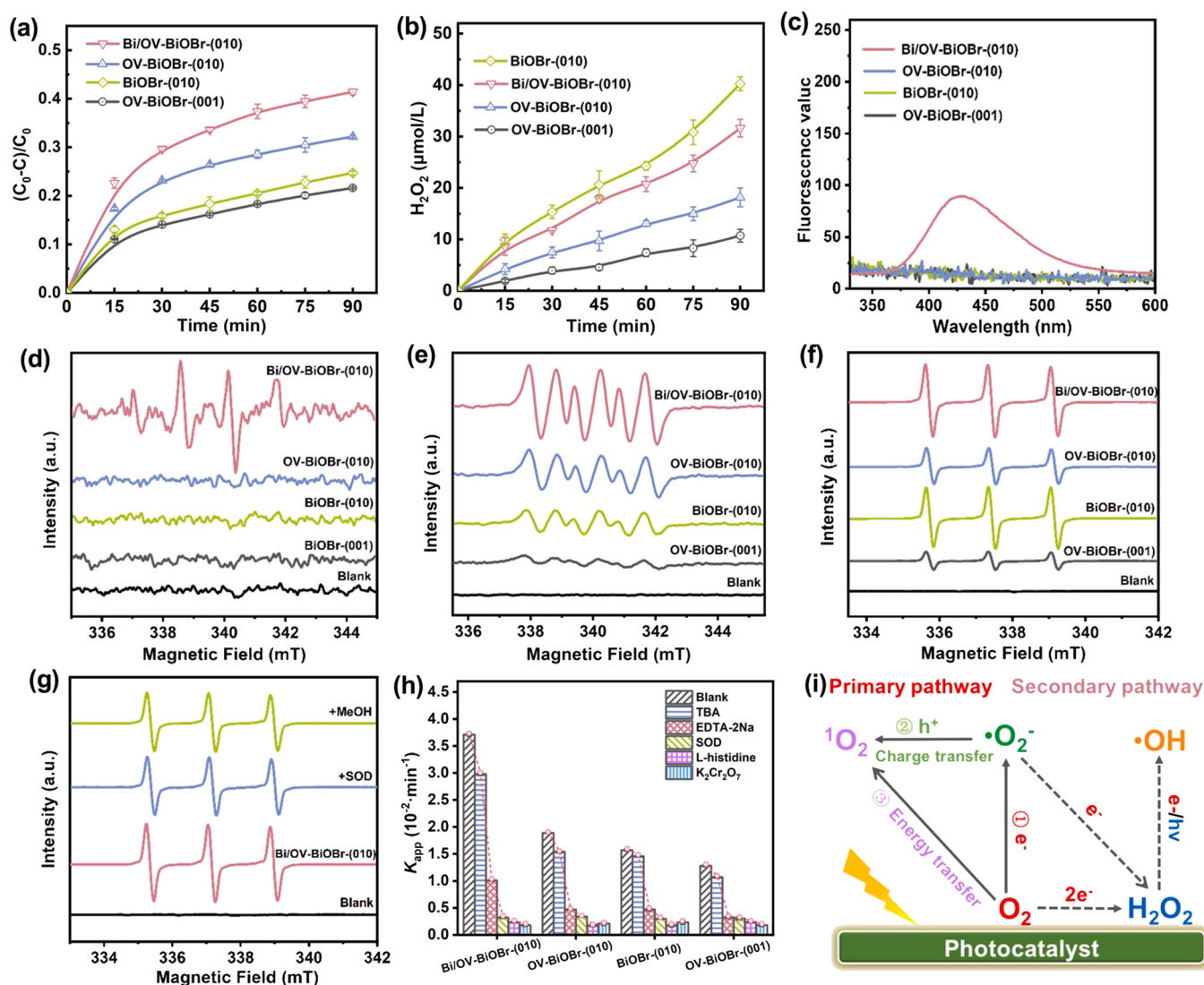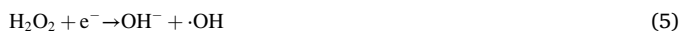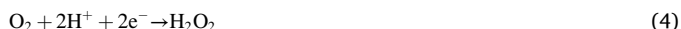

Fig. 5. (a) Transformation percentage of NBT, (b) H_2O_2 generation in the time-course variation (c) TAOH fluorescence intensity over as-prepared samples. (d) DMPO-$\cdot OH$ adducts in water, (e) ESR spectra of DMPO-$\cdot O_2^-$ adducts in methanol and (f) TEMP-$^1O_2$ adducts in water over different BiOBr samples after 1 min visible light irradiation. (g) ESR spectra of TEMP-$^1O_2$ adducts over Bi/OV-BiOBr-(010) in presence of SOD/methanol scavenger. (h) Effects of different radical scavenger on the photodegradation rates of SMX. (h) The scheme of ROS generation and transformation on the surface of Bi/OV-BiOBr-(010) with illumination.

of generated ·OH over Bi/OV-BiOBr-(010) might originate from the oxidation of OH⁻/H_2O by holes (Eq. (7)) [50].

$$O_2 + e^- \rightarrow \cdot O_2^- \tag{1}$$

$$\cdot O_2^- + H^+ \rightarrow HO_2 \tag{2}$$

$$HO_2 \cdot + H^+ + e^- \rightarrow H_2O_2 \tag{3}$$

$$O_2 + 2H^+ + 2e^- \rightarrow H_2O_2 \tag{4}$$

$$H_2O_2 + e^- \rightarrow OH^- + \cdot OH \tag{5}$$

$$H_2O_2 + h\nu \rightarrow 2 \cdot OH \tag{6}$$

$$H_2O + h^+ \rightarrow \cdot OH + H^+ \tag{7}$$

$$^3O_2 \rightarrow {}^1O_2 \tag{8}$$

$$\cdot O_2^- + h^+ \rightarrow 2 {}^1O_2 \tag{9}$$

ESR measurement was further conducted to directly observe the ROS generation. As shown in Fig. 5d–f, Bi/OV-BiOBr-(010) has the strongest ESR signals (i.e., the signals of DMPO-·O_2^-, DMPO-·OH, TEMP-$^1O_2$ adducts), suggesting the significantly improved ROS generation efficiency. This may be primarily attributed to the improved charge transfer-separation and O_2 activation enabled by Bi-OV dual active sites. Notably, only Bi/OV-BiOBr-(010) exhibit a DMPO-·OH quartet signal while no discernable DMPO-·OH signal was observed for the rest three BiOBr catalysts. This agrees well with the TAOH fluorescence results in Fig. 5c. As expected, DMPO-·O_2^- signal intensity follows the order of Bi/ OV-BiOBr-(010) > OV-BiOBr-(010) > BiOBr-(010) > OV-BiOBr-(001), consistent with the results of NBT transformation efficiency in Fig. 5a. Note that the order of TEMP-$^1O_2$ signal is different from that of DMPO-·O_2^- signal, where BiOBr-(010) show a higher TEMP-$^1O_2$ signal but a lower DMPO-·O_2^- signal than OV-BiOBr-(010). The indicates that constructing surface OV may alter O_2 activation mechanisms for BiOBr-(010). Generally, ·O_2^- generation is a one electron transfer process for O_2 reduction (Eq. (1)), while $^1O_2$ can be generated through two pathways (energy transfer (Eq. (8)) and charge transfer pathways (Eq. (9))). The confined layered BiOBr-(010) nanosheets have considerable interlayer binding energy, and this would result in high exciton generation but low electron yield [33]. Whereas, the surface OV exerts a positive effect in dissociating excitons into free charge carriers [33]. In this case, it is reasonable that BiOBr-(010) shows a higher TEMP-$^1O_2$ signal but lower DMPO-·O_2^- signal with respect to OV-BiOBr-(010). To determine the dominating $^1O_2$ generation mechanism, we monitored the change of TEMP-$^1O_2$ signals for both Bi/OV-BiOBr-(010) and OV-BiOBr-(010) after adding quenchers (i.e., SOD as·O_2^- quencher and methanol (MeOH), as h^+ quencher). After adding quenchers, TEMP-$^1O_2$ signals for OV-BiOBr-(010) barely change (Fig. S7), but those for Bi/OV-BiOBr-(010) are slightly inhibited (Fig. 5g). These results indicate that energy transfer is the dominant $^1O_2$ generation mechanism for both catalysts and that charge transfer also has a detectable contribution to $^1O_2$ generation for Bi/OV-BiOBr-(010). One plausible explanation is that the SPR effect of surface Bi^0 in Bi/OV-BiOBr-(010) may drive hot electrons to the nearby BiOBr. This would improve interfacial charge separation-transfer and thus induce a minor contribution of charge transfer towards $^1O_2$ generation.

The scavenging experiments were further conducted to investigate the primary functional ROS and clarify the O_2 activation pathway. EDTA-2Na, $K_2Cr_2O_7$, SOD, TBA, and L-histidine serve as the scavengers for h^+, e^-, ·O_2^-, ·OH, and $^1O_2$, respectively. As shown in Fig. 5h, SMX photodegradation is remarkably inhibited with the addition of $K_2Cr_2O_7$, SOD, L-histidine, and EDTA-2Na, but TBA addition only slightly suppresses SMX photodegradation. This suggests that e^-, ·O_2^-, $^1O_2$, and h^+ are the primary functional reactive species for SMX photodegradation.

Combining the results of ROS determination, ESR measurement and trapping experiments, the ROS generation and conversion pathways for Bi/OV-BiOBr-(010) activating molecular O_2 were proposed in Fig. 5i. Under irradiation, Bi/OV-BiOBr-(010) is excited to generate electron-hole pairs, enabling O_2 molecular activation to massive ROS. Bi/OV-BiOBr-(010) preferentially activate molecular O_2 to generate ·O_2^- via conduction band reduction and generate $^1O_2$ via energy transfer. Benefitting from the efficient charge separation and transfer induced by the surface OVs and Bi metals, a small proportion of the generated ·O_2^- is oxidized to $^1O_2$ by the photoexcited holes via charge transfer. Meanwhile, ·O_2^- is partially reduced to H_2O_2 and further to·OH via two one-step electron reduction.

3.5. Photocatalytic performance

To understand the effect of O_2 dissociation on the degradation of refractory pollutants, the photocatalytic SMX degradation kinetics for all prepared BiOBr samples were compared. As displayed in Fig. 6a, dark adsorption has a minor effect on SMX removal. Under illumination, Bi/ OV-BiOBr-(010) completely remove SMX in 90 min, but less than 80 % of SMX is removed by OV-BiOBr-(001), OV-BiOBr-(010), and BiOBr-(010). As shown in Fig. 6b, the pseudo first-order rate constants (k_{app}) are in the order of Bi/OV-BiOBr-(010) (3.71×10^{-2} min^{-1}) > OV-BiOBr-(010) (1.89×10^{-2} min^{-1}) > BiOBr-(010) (1.52×10^{-2} min^{-1}) > OV-BiOBr-(001) (1.28×10^{-2} min^{-1}). Since the optical thickness (τ) is an important deterministic factor for the photocatalytic activity [51], the performance of the catalysts under the empirical optimal τ ($\sim$ 3) as reported in the literatures [52,53]) were compared. The detailed calculation methods for τ are provided in Text S6. Under τ of 3, the catalyst loadings of OV-BiOBr-(001), OV-BiOBr-(010), Bi/OV-BiOBr-(010), and BiOBr-(010) were calculated to be 1.43, 0.58, 0.73, and 3.74 g/L, respectively. As shown in Fig. 6d, the corresponding k_{app} values are in the order of Bi/OV-BiOBr-(010) (3.28×10^{-2} min^{-1}) > OV-BiOBr-(001) (3.04×10^{-2} min^{-1}) > BiOBr-(010) (2.45×10^{-2} min^{-1}) > OV-BiOBr-(010) (2.27×10^{-2} min^{-1}). Despite a relatively small catalyst loading, the Bi/OV-BiOBr-(010) still has the highest k_{app}. This result further supports the superiority of the Bi-OV dual active sites. To better understand the effects of catalyst loadings on photocatalytic kinetics, the SMX degradation kinetics under different loadings (0.1–1.0 g/L) for all the catalysts were compared (Fig. S8). Very surprisingly, as catalyst loadings increased from 0.1 to 1.0 g/L, the rate constant for Bi/OV-BiOBr-(010) continuously drops but those for the other three catalysts gradually increase (Fig. S9). Bi/OV-BiOBr-(010) even exhibits a k_{app} of 3.60×10^{-2} min^{-1} with the catalyst loading as low as 0.1 g/L. This implies that Bi/OV-BiOBr-(010) performs even better with less catalyst loadings, indicating the high efficiency and the promising application potentials. Besides, the apparent quantum yield (AQY) of the four photocatalysts, which is defined as the ratio of the number of photos that cause reaction to the number of incident photons to the system, was calculated by Eq. S8. Results in Fig. S10 shows that the order of AQY (Bi/OV-BiOBr-010 (7.19 %) > OV-BiOBr-010 (6.56 %) > OV-BiOBr-001 (5.09 %) > BiOBr-010 (4.98 %)) consists well with the k_{app} order for SMX photodegradation. Apparently, Bi/OV-BiOBr-(010) exhibits both higher photocatalytic kinetics and AQY for SMX photodegradation. This implies Bi/OV-BiOBr-(010) can more effectively utilize the incident photons for efficient degradation of organic pollutants, further suggesting the promising application potentials. Combining these results and the characterization analysis above, it can be concluded that (i) BiOBr has a facet-dependent photo-reactivity towards SMX degradation, and BiOBr with (010) facets outperformed that with (001) facets. (ii) Surface OV decoration can effectively improve the photo utilization efficiency of BiOBr, which can be further enhanced by Bi metal deposition. The synergistic effects between surface OVs and metallic Bi would be intricately discussed in Section 3.6.

The photocatalytic efficiency of Bi/OV-BiOBr-(010) was also evaluated by the comparison with the commercial TiO_2, ZnO, CdS and the
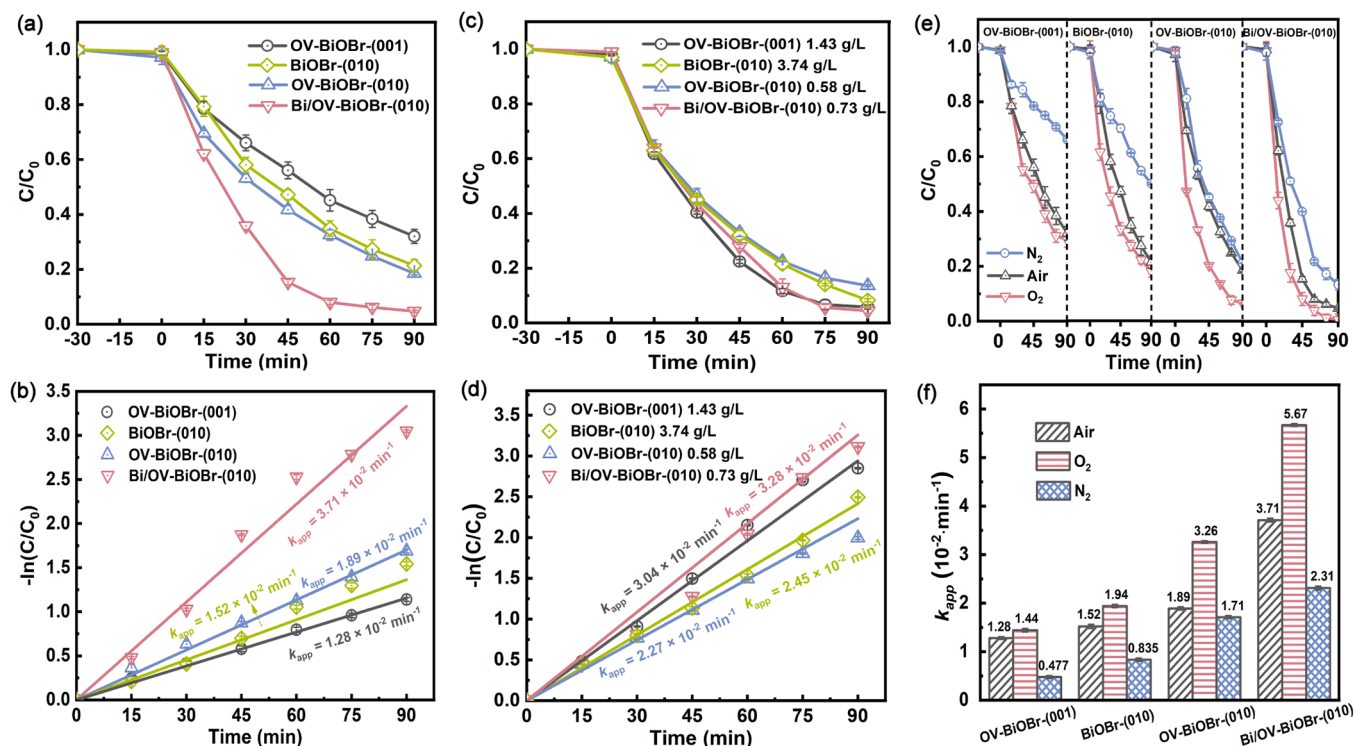
Fig. 6. Photocatalytic performance of the as-prepared samples for SMX degradation. (a) Photocatalytic degradation of SMX and (b) the corresponding kinetic constants. (c) Photocatalytic degradation of SMX in the suspension catalytic system with the identical optical thickness of 3 (the catalyst loadings of OV-BiOBr-(001), OV-BiOBr-(010), Bi/OV-BiOBr-(010), and BiOBr-(010) were calculated to be 1.43, 0.58, 0.73, and 3.74 g/L, respectively) and (d) the corresponding kinetic constants. (e) The photocatalytic SMX degradation curves in different atmospheres and (f) the corresponding kinetic constants.

homemade g-C_3N_4 photocatalysts (Fig. S11). Amongst, Bi/OV-BiOBr-(010) shows an outstanding photocatalytic performance, with a k_{app} even over three times that of the two well-known TiO_2 (0.80×10^{-2} min^{-1}) and ZnO (1.03×10^{-2} min^{-1}) photocatalysts. Compared to other reported bismuth-based photocatalysts, Bi/OV-BiOBr-(010) was also among the most reactive photocatalysts (Table S6). In addition, TOC analysis was conducted to substantiate the effective photocatalytic mineralization of SMX. About 31 % of the TOC can be removed when SMX is completely degraded in 90 min and nearly 50 % of the TOC can be removed by extending the illumination time to 6 h (Fig. S12). Moreover, Bi/OV-BiOBr-(010) retains nearly 91 % and 80 % photocatalytic degradation efficiencies after four and eight cycles, respectively (Fig. S13). The crystal structure, sheet-shaped structure, surface OVs, and metallic Bi of the used Bi/OV-BiOBr-(010) after multicycles have no obvious change, suggesting the desirable stability and reusability (Fig. S14).

The effect of atmospheric O_2 on the photocatalysis is further studied by bubbling O_2 and N_2, with air atmosphere as the control condition. For all prepared photocatalysts, O_2 bubbling noticeably promotes SMX photodegradation while N_2 bubbling exerts an inhibition effect (Figs. 6e, 6f). Since O_2 bubbling is a green method and is simple to operate, combining O_2 bubbling with defective catalysts may be a promising strategy to remove refractory pollutants in practice. Notably, the ratio of k_{app} increase by O_2 bubbling for the prepared catalysts followed the same order as the k_{app}. The k_{app} values of BiOBr-(001), BiOBr-(010), OV-BiOBr-(010), and Bi/OV-BiOBr-(010) increase by 12.5 %, 27.6 %, 42.0 %, and 52.8 %, respectively. These results further supported the synergistic effects of surface OVs and Bi metals on facilitating O_2 activation for SMX degradation. However, the inhibition order caused by N_2 bubbling is not in conformity with the promotion order caused by O_2 bubbling as expected. Compared to BiOBr-(001) and BiOBr-(010), a weaker inhibition was observed for OV-BiOBr-(010) and Bi/OV-BiOBr-(010) upon N_2 bubbling. This suggests that there are other

mechanisms responsible for SMX photodegradation besides the O_2 activation pathway (i.e., the hole direct oxidation pathway).

3.6. Photocatalytic mechanism

According to the theoretical and experimental results, the photocatalytic mechanisms of molecular oxygen activation on Bi/OV-BiOBr-(010) are illustrated in Fig. 7. A facet-dependent synergistic mechanism of Bi-OV dual active sites on Bi/OV-BiOBr-(010) was proposed. Upon illumination, electrons are excited and migrated from VB to CB, leaving holes at the VB. In presence of OVs, the electron transition is separated into two continuous steps. The electrons on VB of BiOBr-(010) are firstly excited to the intermediate defect levels formed by the OVs and BrVs, and are excited to the CB of BiOBr-(010) afterwards. This two-
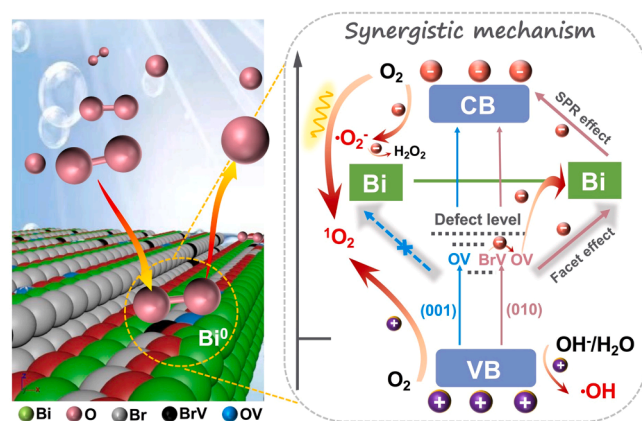
Fig. 7. Proposed photocatalytic mechanism of Bi/OV-BiOBr-(010) for molecular O_2 activation and synergy of Bi-OV dual active site.

step electron transition path ease the path of electrons hopping from VB to CB when comparing with bare BiOBr-(010). Additionally, the intermediate defect level provides a more competent photoelectron-trapping center to inhibit the recombination of charge carriers, as confirmed in Fig. 4. The BrVs would transfer part of the localized electrons to the neighboring OVs, rendering the OVs to be electron-"richer". Because of the open channel topology of BiOBr (010) facet with O, Br, and Bi atoms exposed, the surface Bi^{3+} can be easily reduced to metallic Bi by the delocalized electrons around the OVs. The generated Bi metals will inject the SPR hot electrons into the CB of BiOBr and form the Schottky barrier at the Bi-BiOBr interface, further improving the generation and separation of photoinduced electron-hole pairs. The electrons accumulated on the CB will reduce O_2 to $\cdot O_2^-$ as confirmed in ROS detection although the E_{CB} (-0.28 eV) of Bi/OV-BiOBr-(010) is slightly less negative than the E^0 of of $O_2/\cdot O_2^-$ (-0.33 V/SHE). Since the CB has a certain breadth, so electrons can be photoexicted to higher levels of CB and thus reduce O_2 to $\cdot O_2^-$ [43]. The generated $\cdot O_2^-$ can be further reduced to H_2O_2 by electrons or be oxidized to $^1O_2$ by holes. Meanwhile, the electrons on the CB can induce the $^1O_2$ generation from the triplet ground state O_2 through the energy transfer pathway. The holes accumulated on the VB will oxide OH^-/H_2O to $\cdot OH$ because of the more positive E_{VB} (2.85 eV) than the E^0 of $\cdot OH/OH^-$ (1.99 V/SHE) and $\cdot OH/H_2O$ (2.27 V/SHE) [50]. The holes, and the generated ROS (including $\cdot O_2^-$, $^1O_2$, and $\cdot OH$) continuously degrade SMX. Due to the close structure of BiOBr-(001), only mono OVs can be introduced on the (001) facet. The geometry-flexible structure of (010) facet, with alternatively arranged Bi, O, and Bi atoms, allows the simultaneous formation of OVs and BrVs on the (010) facet. BrVs provides extra localized electrons to OVs for in-situ partial reduction of Bi^{3+} to Bi^0, and this enables metallic Bi and surface OVs to work as Bi-OV dual active sites. On one hand, both the deposited Bi metal and OVs serve as the active centers for adsorbing and activating O_2 molecules, substantially lowing the adsorption energy of O_2 from -0.28 to -4.34 eV and increasing O-O bond lengths of adsorbed O_2 from 1.26 to 1.55 Å. As a result, the enhanced O_2 adsorption, rapid O_2 dissociation, and promoted ROS production are achieved. On the other hand, Bi metals, as both the electron acceptors and donors, simultaneously accept the driven localized electrons from the OVs and inject the hot electrons into BiOBr. This particular electron transfer pattern promotes the interfacial charge separation-transfer and induces more produced ROS. Benefitting from the geometry-flexible structure of (010) facet and the synergy of Bi-OV dual active sites in O_2 adsorption-activation and charge separation-transfer, Bi/O-V-BiOBr-(010) exhibits superior SMX degradation over other three prepared BiOBr nanosheets.

4. Conclusions

A series of BiOBr nanosheets with dominantly exposed (001) and (010) facets were synthesized via a facile solvothermal route. The (010) facets were identified as the preferred facets, and the superiority was significant enhanced by the simultaneous creation of metallic Bi and surface OVs. Experimental characterization and DFT calculation confirmed that Bi metals and OVs worked synergistically to i) substantially reduce the adsorption energy and increase O—O bond lengths of adsorbed O_2, resulting in enhanced O_2 adsorption, rapid O_2 dissociation, and promoted ROS production, and (ii) establish a particular charge transfer pattern between metallic Bi and OVs, which facilitates the interfacial charge separation-transfer. As a result, BiOBr-(010) with Bi-OV dual active sites exhibits superior O_2 activation and SMX degradation over BiOBr-(010) with mono OVs, bare BiOBr-(010), and other well-known photocatalysts. This study unravels the intrinsic facet-dependent reactivity and opens the possibilities to simultaneously include multiple active sites into geometry-flexible photocatalysts by rationally manipulating surface atoms for environmental remediation.

CRediT authorship contribution statement

Guanglan Di: Data curation, Writing – original draft. **Langlang Wang:** Data curation, Writing – original draft. **Xuede Li:** Supervision, Project administration, Funding acquisition. **Xiaoli Zhao:** Writing – review & editing. **Guangpeng Yang:** Methodology, Software. **Lei Huang:** Software. **Zefang Chen:** Methodology, Writing – review & editing. **John Crittenden:** Supervision, Writing – review & editing.

Declaration of Competing Interest

The authors declare that they have no known competing financial interests or personal relationships that could have appeared to influence the work reported in this paper.

Data Availability

No data was used for the research described in the article.

Appendix A. Supporting information

Supplementary data associated with this article can be found in the online version at doi:10.1016/j.apcatb.2022.122349.

References

[1] C.W. Zhang, C.P. Kong, P.G. Tratnyek, C.Y. Qin, Generation of reactive oxygen species and degradation of pollutants in the Fe^{2+}/O_2/tripolyphosphate system: regulated by the concentration ratio of Fe^{2+} and tripolyphosphate, Environ. Sci. Technol. 56 (2022) 4367–4376.

[2] H.Y. Zhan, Q.X. Zhou, M.M. Li, R.R. Zhou, Y.S. Mao, P.F. Wang, Photocatalytic O_2 activation and reactive oxygen species evolution by surface B—N bond for organic pollutants degradation, Appl. Catal. B Environ. 310 (2022), 121329.

[3] Z.H. Xie, C.S. He, H.Y. Zhou, L.L. Li, Y. Liu, Y. Du, W. Liu, Y. Mu, B. Lai, Effects of molecular structure on organic contaminants' degradation efficiency and dominant ROS in the advanced oxidation process with multiple ROS, Environ. Sci. Technol. 56 (2022) 8784–8795.

[4] A. Jawad, K. Zhan, H.B. Wang, A. Shahzad, Z.H. Zeng, J. Wang, X.Q. Zhou, H. Ullah, Z.L. Chen, Z.Q. Chen, Tuning of persulfate activation from a free radical to a nonradical pathway through the incorporation of Non-Redox agnesium xide, Environ. Sci. Technol. 54 (2020) 2476–2488.

[5] X.Y. Amina, K. Si, Y.B. Wu, B. Si, Yousaf, Mechanistic insights into the reactive radicals-assisted degradation of sulfamethoxazole via calcium peroxide activation by manganese-incorporated iron oxide-graphene nanocomposite: formation of radicals and degradation pathway, Chem. Eng. J. 384 (2020), 123360.

[6] M.M. Li, P.F. Wang, Z.Z. Ji, Z.R. Zhou, Y.G. Xia, Y. Li, S.H. Zhan, Efficient photocatalytic oxygen activation by oxygen-vacancy-rich CeO_2-based heterojunctions: synergistic effect of photoexcited electrons transfer and oxygen chemisorption, Appl. Catal. B Environ. 289 (2021), 120020.

[7] Z.P. Yang, Y.B. Shi, H. Li, C.L. Mao, X.B. Wang, X.F. Liu, X. Liu, L.Z. Zhang, Oxygen and chlorine dual vacancies enable photocatalytic O_2 dissociation into monatomic reactive oxygen on BiOCl for refractory aromatic pollutant removal, Environ. Sci. Technol. 56 (2022) 3587–3595.

[8] Q. Li, F.T. Li, Recent advances in molecular oxygen activation via photocatalysis and its application in oxidation reactions, Chem. Eng. J. 421 (2021) 129915.

[9] Z.R. Zhou, Z.R. Shen, C.L. Song, M.M. Li, H. Li, S.H. Zhan, Boosting the activation of molecular oxygen and the degradation of tetracycline over high loading Ag single atomic catalyst, Water Res. 201 (2021), 117314.

[10] J.Y. Zhang, J.W. Liu, Light-activated nanozymes: catalytic mechanisms and applications, Nanoscale 12 (2020) 2914–2923.

[11] X.Y. Huang, J.T. Groves, Oxygen activation and radical transformations in heme proteins and metalloporphyrins, Chem. Rev. 118 (2018) 2491–2553.

[12] S.J. Liu, F.T. Li, Y.L. Li, Y.J. Hao, Xj Wang, B. Li, R.H. Liu, Fabrication of ternary g-C_3N_4/Al_2O_3/ZnO heterojunctions based on cascade electron transfer toward molecular oxygen activation, Appl. Catal. B Environ. 212 (2017) 115–128.

[13] H. Zhao, X. Liu, Y.M. Dong, Y.M. Xia, H.J. Wang, A special synthesis of BiOCl photocatalyst for efficient pollutants removal: new insight into the band structure regulation and molecular oxygen activation, Appl. Catal. B Environ. 256 (2019), 117872.

[14] J.Y. Li, X.A. Dong, Y.J. Sun, W.L. Cen, F. Dong, Facet-dependent interfacial charge separation and transfer in plasmonic photocatalysts, Appl. Catal. B Environ. 226 (2018) 269–277.

[15] B. Zeng, S.Y. Wang, Y.Y. Gao, G.N. Li, W.M. Tian, J. Meeprasert, H. Li, H.C. Xie, F. T. Fan, R.G. Li, C. Li, Interfacial modulation with aluminum oxide for efficient plasmon-induced water oxidation, Adv. Funct. Mater. 31 (2021) 2005688.

[16] R. Verma, R. Belgamwar, V. Polshettiwar, Plasmonic photocatalysis for CO2 conversion to chemicals and fuels, ACS Mater. Lett. 3 (2021) 574–598.

[17] K. Shoueir, S. Kandil, H. El-hosainy, M. El-Kemary, Tailoring the surface reactivity of plasmonic Au@TiO2 photocatalyst bio-based chitosan fiber towards cleaner of harmful water pollutants under visible-light irradiation, J. Clean. Prod. 230 (2019) 383–393.

[18] S. Tiewcharoen, C. Warakulwit, V. Lapeyre, P. Garrigue, L. Fourier, C. Elissalde, S. Buffiere, P. Legros, M. Gayot, J. Limtrakul, A. Kuhn, Anisotropic metal deposition on TiO2 particles by electric-field-induced charge separation, Angew. Chem. Int. Ed. 56 (2017) 11431–11435.

[19] X.Z. Liang, P. Wang, Y.G. Gao, H.N. Huang, F.X. Tong, Q.Q. Zhang, Z.Y. Wang, Y. Y. Liu, Z.K. Zheng, Y. Dai, B.B. Huang, Design and synthesis of porous M-ZnO/ CeO2 microspheres as efficient plasmonic photocatalysts for nonpolar gaseous molecules oxidation: insight into the role of oxygen vacancy defects and M = Ag, Au nanoparticles, Appl. Catal. B Environ. 260 (2020), 118151.

[20] X.Z. Zhu, H.L. Jia, X.M. Zhu, S. Cheng, X.L. Zhuo, F. Qin, Z. Yang, J.F. Wang, Selective Pd deposition on Au nanobipyramids and Pd site-dependent plasmonic photocatalytic activity, Adv. Funct. Mater. 27 (2017) 1700016.

[21] M. Sayed, J.G. Yu, G. Liu, M. Jaroniec, Non-noble plasmonic metal-based photocatalysts, Chem. Rev. 122 (2022) 10484–10537.

[22] F. Dong, T. Xiong, S. Yan, H.Q. Wang, Y.J. Sun, Y.X. Zhang, H.W. Huang, Z.B. Wu, Facets and defects cooperatively promote visible light plasmonic photocatalysis with Bi nanowires@BiOCl nanosheets, J. Catal. 344 (2016) 401–410.

[23] P. Kong, H. Tan, T.Y. Lei, J. Wang, W.J. Yan, R.Y. Wang, E.R. Waclawik, Z. F. Zheng, Z. Li, Oxygen vacancies confined in conjugated polyimide for promoted visible-light photocatalytic oxidative coupling of amines, Appl. Catal. B Environ. 272 (2020), 118964.

[24] X.W. Li, W.D. Zhang, W. Cui, J.Y. Li, Y.J. Sun, G.M. Jiang, H.W. Huang, Y.X. Zhang, F. Dong, Reactant activation and photocatalysis mechanisms on Bi-metal@Bi2GeO5 with oxygen vacancies: a combined experimental and theoretical investigation, Chem. Eng. J. 370 (2019) 1366–1375.

[25] P. Chen, H.J. Liu, Y.J. Sun, J.Y. Li, W. Cui, L. Wang, W.D. Zhang, X.Y. Yuan, Z. M. Wang, Y.X. Zhang, F. Dong, Bi metal prevents the deactivation of oxygen vacancies in Bi2O2CO3 for stable and efficient photocatalytic NO abatement, Appl. Catal. B Environ. 264 (2020) 118545.

[26] X. Zhou, J. Zhang, X.M. Wang, T.Q. Tan, R.M. Fang, S. Chen, F. Dong, Efficient NO removal and photocatalysis mechanism over Bi-metal@Bi2O2[BO2(OH)] with oxygen vacancies, J. Hazard. Mater. 436 (2022), 129271.

[27] H. Li, J. Li, Z.H. Ai, F.L. Jia, L.Z. Zhang, Oxygen vacancy-mediated photocatalysis of BiOCl: reactivity, selectivity, and perspectives, Angew. Chem. Int. Ed. 57 (2018) 122–138.

[28] H.G. Zhang, L.Y. Zhao, L. Wang, J. Hao, X.C. Meng, Fabrication of oxygen-vacancy-rich black-BiOBr/BiOBr heterojunction with enhanced photocatalytic activity, J. Mater. Sci. 55 (2020) 10785–10795.

[29] W.H. Zhang, Z.Y. Bian, Y.Y. Peng, H.Y. Tang, H. Wang, Dual-function oxygen vacancy of BiOBr intensifies pollutant adsorption and molecular oxygen activation to remove tetracycline hydrochloride, Chem. Eng. J. 451 (2023), 138731.

[30] M. Shi, G.N. Li, J.M. Li, X. Jin, X.P. Tao, B. Zeng, E.A. Pidko, R.G. Li, C. Li, Intrinsic facet-dependent reactivity of well-defined BiOBr nanosheets on photocatalytic water splitting, Angew. Chem. Int. Ed. 59 (2020) 6590–6595.

[31] D.N. Liu, D.Y. Chen, N.J. Li, Q.F. Xu, H. Li, J.H. He, J.M. Lu, Surface engineering of g-C3N4 by stacked BiOBr sheets rich in oxygen vacancies for boosting photocatalytic performance, Angew. Chem. Int. Ed. 59 (2020) 4519–4524.

[32] X.J. Ren, M.C. Gao, Y.F. Zhang, Z.Z. Zhang, X.Z. Cao, B.Y. Wang, X.X. Wang, Photocatalytic reduction of CO2 on BiOX: effect of halogen element type and surface oxygen vacancy mediated mechanism, Appl. Catal. B Environ. 274 (2020), 119061.

[33] H. Wang, D.Y. Yong, S.C. Chen, S.L. Jiang, X.D. Zhang, W. Shao, Q. Zhang, W. S. Yan, B.C. Pan, Y. Xie, Oxygen-vacancy-mediated exciton dissociation in BiOBr for boosting charge-carrier-involved molecular oxygen activation, J. Am. Chem. Soc. 140 (2018) (5320-5320).

[34] H.P. Li, T.X. Hu, N. Du, R.J. Zhang, J.Q. Liu, W.G. Hou, Wavelength-dependent differences in photocatalytic performance between BiOBr nanosheets with

[35] Y.W. Mi, H.P. Li, Y.F. Zhang, N. Du, W.G. Hou, Synthesis and photocatalytic activity of BiOBr nanosheets with tunable crystal facets and sizes, Catal. Sci. Technol. 8 (2018) 2588–2597.

[36] G.L. Di, Z.L. Zhu, Q.H. Huang, H. Zhang, J.Y. Zhu, Y.L. Qiu, D.Q. Yin, J.F. Zhao, Targeted modulation of g-C3N4 photocatalytic performance for pharmaceutical pollutants in water using ZnFe-LDH derived mixed metal oxides: structure-activity and mechanism, Sci. Total Environ. 650 (2019) 1112–1121.

[37] V. Klassen, D. Marchlngton, E. McGowan, H2O2 determination by the I3⁻ method and by KMnO4 titration, Anal. Chem. 66 (1994) 2921–2925.

[38] R.M. Baena-Nogueras, E. Gonzalez-Mazo, P.A. Lara-Martin, Photolysis of antibiotics under simulated sunlight irradiation: identification of photoproducts by high-resolution mass spectrometry, Environ. Sci. Technol. 51 (2017) 3148–3156.

[39] C.M. Dai, S. Li, Y.P. Duan, K.H. Leong, S.G. Liu, Y.L. Zhang, L. Zhou, Y.J. Tu, Mechanisms and product toxicity of activated carbon/peracetic acid for degradation of sulfamethoxazole: implications for groundwater remediation, Water Res. 216 (2022), 118347.

[40] X.L. Wu, Y.H. Ng, L. Wang, Y. Du, S.X. Dou, R. Amal, J. Scott, Improving the photo-oxidative capability of BiOBr via crystal facet engineering, J. Mater. Chem. A 5 (2017) 8117–8124.

[41] X.J. Tong, X. Cao, T. Han, W.C. Cheong, R. Lin, Z. Chen, D.S. Wang, C. Chen, Q. Peng, Y.D. Li, Convenient fabrication of BiOBr ultrathin nanosheets with rich oxygen vacancies for photocatalytic selective oxidation of secondary amines, Nano Res. 12 (2019) 1625–1630.

[42] H.P. He, J.L. Cao, X.C. Fei, N. Duan, High-temperature annealing of ZnO nanoparticles increases the dissolution magnitude and rate in water by altering O vacancy distribution, Environ. Int. 130 (2019), 104930.

[43] X.A. Dong, W.D. Zhang, Y.J. Sun, J.Y. Li, W.L. Cen, Z.H. Cui, H.W. Huang, F. Dong, Visible-light-induced charge transfer pathway and photocatalysis mechanism on Bi semimetal@defective BiOBr hierarchical microspheres, J. Catal. 357 (2018) 41–50.

[44] X.J. Tong, X. Cao, T. Han, W.C. Cheong, R. Lin, Z. Chen, D.S. Wang, C. Chen, Q. Peng, Y.D. Li, Convenient fabrication of BiOBr ultrathin nanosheets with rich oxygen vacancies for photocatalytic selective oxidation of secondary amines, Nano Res. 12 (2019) 1625–1630.

[45] S. Wu, W. Sun, J. Sun, Z.D. Hood, S.Z. Yang, L. Sun, P.R.C. Kent, M.F. Chisholm, Surface reorganization leads to enhanced photocatalytic activity in defective BiOCl, Chem. Mater. 30 (2018) 5128–5136.

[46] A. Ishikawa, T. Takata, J.N. Kondo, M. Hara, H. Kobayashi, K. Domen, Oxysulfide Sm2Ti2S2O5 as a stable photocatalyst for water oxidation and reduction under visible light irradiation (λ ≤ 650 nm), J. Am. Chem. Soc. 124 (2002) 13547–13553.

[47] Y. Wang, X.Q. Liu, J. Liu, B. Han, X.Q. Hu, F. Yang, Z.W. Xu, Y.C. Li, S.R. Jia, Z. Li, Y.L. Zhao, Carbon quantum dot implanted graphite carbon nitride nanotubes: excellent charge separation and enhanced photocatalytic hydrogen evolution, Angew. Chem. Int. Ed. 57 (2018) 5765–5771.

[48] J.H. Zheng, L. Zhang, Incorporation of CoO nanoparticles in 3D marigold flower-like hierarchical architecture MnCo2O4 for highly boosting solar light photo-oxidation and reduction ability, Appl. Catal. B Environ. 237 (2018) 1–8.

[49] X. Xu, J. Wang, T. Chen, N. Yang, S.Y. Wang, X. Ding, H. Chen, Deep insight into ROS mediated direct and hydroxylated dichlorination process for efficient photocatalytic sodium pentachlorophenate mineralization, Appl. Catal. B Environ. 296 (2021) 120352.

[50] G.L. Di, Z.L. Zhu, H. Zhang, J.Y. Zhu, Y.L. Qiu, D.Q. Yin, S. Küppers, Visible-light degradation of sulfonamides by Z-scheme ZnO/g-C3N4 heterojunctions with amorphous Fe2O3 as electron mediator, J. Colloid Interface Sci. 538 (2019) 256–266.

[51] G.L. Puma, Modeling of thin-film alurry photocatalytic reactors affected by radiation scattering, Environ. Sci. Technol. 37 (2003) 5783–5791.

[52] I. Grčić, G.L. Puma, Six-flux absorption-scattering models for photocatalysis under wide-spectrum irradiation sources in annular and flat reactors using catalysts with different optical properties, Appl. Catal. B Environ. 211 (2017) 222–234.

[53] R. Acosta-Herazo, M.Á. Mueses, G.L. Puma, F. Machuca-Martínez, Impact of photocatalyst optical properties on the efficiency of solar photocatalytic reactors rationalized by the concepts of initial rate of photon absorption (IRPA) dimensionless boundary layer of photon absorption and apparent optical thickness, Chem. Eng. J. 356 (2019) 839–849.

dominant exposed (001) and (010) facets, Appl. Catal. B Environ. 187 (2016) 342–349.